Scattering and absorption property database for nonspherical ice particles in the near- through far-infrared spectral region

Ping Yang, Heli Wei, Hung-Lung Huang, Bryan A. Baum, Yong X. Hu, George W. Kattawar, Michael I. Mishchenko, and Qiang Fu

The single-scattering properties of ice particles in the near- through far-infrared spectral region are computed from a composite method that is based on a combination of the finite-difference time-domain technique, the T-matrix method, an improved geometrical-optics method, and Lorenz–Mie theory. Seven nonspherical ice crystal habits (aggregates, hexagonal solid and hollow columns, hexagonal plates, bullet rosettes, spheroids, and droxtals) are considered. A database of the single-scattering properties for each of these ice particles has been developed at 49 wavelengths between 3 and 100 μm and for particle sizes ranging from 2 to 10,000 μm specified in terms of the particle maximum dimension. The spectral variations of the single-scattering properties are discussed, as well as their dependence on the particle maximum dimension and effective particle size. The comparisons show that the assumption of spherical ice particles in the near-IR through far-IR region is generally not optimal for radiative transfer computation. Furthermore, a parameterization of the bulk optical properties is developed for mid-latitude cirrus clouds based on a set of 21 particle size distributions obtained from various field campaigns.   © 2005 Optical Society of America

OCIS codes: 010.1310, 010.1290, 290.5850, 290.1090, 300.6170, 260.3060.

1. Introduction

The radiative properties of ice clouds have been studied from various perspectives.[1–8] In particular, substantial research efforts have been focused on the optical properties of ice particles.[9–21] In the past decade, numerous techniques were developed to use high-spectral-resolution IR interferometer measurements for the determination of cloud properties, e.g., that developed by Smith *et al.*[22] Most of these retrieval methods consider measurements primarily within the 8–12 μm atmospheric window region.[23–28] To infer cloud optical thickness or effective particle size, information is required on the bulk scattering properties of these clouds. The single-scattering parameters of ice particles used in the previous studies are generally based on either those of equivalent ice spheres[27,28] or those of pristine hexagonal ice columns and plates.[2,3,19,21]

Various particle morphologies including complex bullet rosettes and aggregates have been observed frequently in cirrus clouds.[29] To account for these ice particle habits in both IR radiative transfer computations and remote sensing applications, more-comprehensive data sets of the single-scattering properties of ice particles are required. This study reports on the development of a comprehensive set of the scattering and absorption properties for seven nonspherical ice particle shapes, or habits, in the near-IR through far-IR spectral region from 3 to 100 μm. The specific ice particle shapes include hexagonal plates, hexagonal solid and hollow columns, aggregates, three-dimensional (3D) bullet rosettes, spheroids, and droxtals. The present scattering computations are carried out for particle maximum dimensions ranging from 2 to 10,000 μm. The single-scattering properties of the aforementioned ice par-

P. Yang (pyang@ariel.met.tamu.edu) and H. Wei are with the Department of Atmospheric Sciences, Texas A&M University, College Station, Texas 77843. H.-L. Huang is with the Cooperative Institute for Meteorological Satellite Studies, University of Wisconsin, Madison, Wisconsin 53706. B. A. Baum and Y. X. Hu are with NASA Langley Research Center, Hampton, Virginia 23681. G. W. Kattawar is with the Department of Physics, Texas A&M University, College Station, Texas 77843. M. I. Mishchenko is with NASA Goddard Institute for Space Studies, New York, New York 10025. Q. Fu is with the Department of Atmospheric Science, University of Washington, Seattle, Washington 98195.

ticles are computed from a composite method[2,3] based on the finite-difference time-domain (FDTD) technique,[12,14,30] an improved geometrical-optics method (IGOM),[17] and the Lorenz–Mie solutions for equivalent spheres. For the single-scattering properties of spheroids, we use the rigorous T-matrix code developed by Mishchenko and Travis[31] for small and moderate size parameters. The size parameter is specified as $x = \pi D/\lambda$, where D is the particle maximum dimension and λ is the wavelength.

The rest of this paper is organized as follows. In Section 2 we provide the details on the present single-scattering calculations. Results for individual ice particles are provided in Section 3. In Section 4 we discuss the bulk scattering properties for midlatitude cirrus clouds, and conclusions are presented in Section 5.

2. Computation of Single-Scattering Properties for Individual Ice Particles

The fundamental single-scattering parameters required for radiative transfer computations are the extinction efficiency, single-scattering albedo, and scattering phase function. The asymmetry factor, which is the first-order moment of the phase function, is also widely used in IR radiative flux computations. These parameters are included in the present database of the single-scattering properties of ice crystals.

The scattering and absorption properties of a particle are determined by the shape and size of the particle, the complex refractive index, and the incident wavelength. The ice particle shapes considered in the present computations are shown in Fig. 1,

Fig. 1. Ice crystal shapes defined for the present scattering calculations.

including aggregates, solid and hollow columns, spheroids, plates, droxtals, and bullet rosettes. For comparison, we also include ice spheres in the present scattering computations. In this study, all these nonspherical ice particles are assumed to be randomly oriented in space. The detailed geometry of the droxtal is defined in Yang et al.[20] and Zhang et al.[32] In addition to their dependence on particle orientations and morphology, the scattering and absorption properties also depend on the particle aspect ratio for a given habit. The aspect ratio α is defined as the ratio of the width of a particle to its length. For a hexagonal column of semiwidth a and length L, the aspect ratio of the hexagonal column is $\alpha = 2a/L$. Following Yang et al.[18] and the references cited therein, we assume the relationship between semiwidth a and length L for a hexagonal column as $a = 0.35L$ when $L < 100$ μm and $a = 0.348L^{0.5}$ for $L \geq 100$ μm. For a hollow hexagonal column, the hollow cavity depth d is assumed to vary randomly between 0 and $L/2$ with an average of $\bar{d} = 0.25L$, and the aspect ratio is the same as that of a column with an identical size. For a plate, we assume the aspect ratio is 1 (i.e., $L = 2a$) for $a \leq 2$ μm and $L = 2.4883a^{0.474}$ for $a \geq 5$ μm; the aspect ratio varies linearly with a for 2 μm $\leq a \leq 5$ μm. For spheroids, we assume that the aspect ratio of a spheroid is 0.5 (the ratio of the length of the short axis to the long or rotationally symmetric axis). For bullet rosettes, the aspect ratio is defined with respect to individual bullet branches. We use the relationship $a = 1.1552L^{0.63}$, where a and L are the semiwidth and length of an individual bullet branch, respectively. The procedure for defining an aggregate has been presented by Yang and Liou.[33] Detailed definitions of the 3D geometry for each habit can be found in Yang et al.[18] and the references therein.

The effective particle size[3,34,35] for an individual ice crystal is defined in this study as follows:

$$D_e(L) = \frac{3}{2} \frac{V(L)}{A(L)}, \qquad (1)$$

where L is the maximum dimension of a nonspherical ice particle and A and V are the projected area and volume of the particle, respectively. Note that the effective size defined in Eq. (1) is proportional to the mean path length of rays in the anomalous diffraction theory or the so-called effective distance.[35] Figure 2 shows a comparison of the D_e–L relationships for various ice habits. For a nonspherical particle, the effective particle size is always smaller than its maximum dimension. For a given maximum dimension, a spherical particle has the largest effective size ($D_e = L$) among all the habits shown in Fig. 1. Given the same maximum dimension and the assumed aspect ratio in this study, the habits may be sorted by descending effective particle size as follows: sphere, droxtal, spheroid, aggregate, solid column, hollow column, bullet rosette, and plate. For small effective particle sizes, owing to the variations of the aspect ratio, the ranking is slightly different. For example,
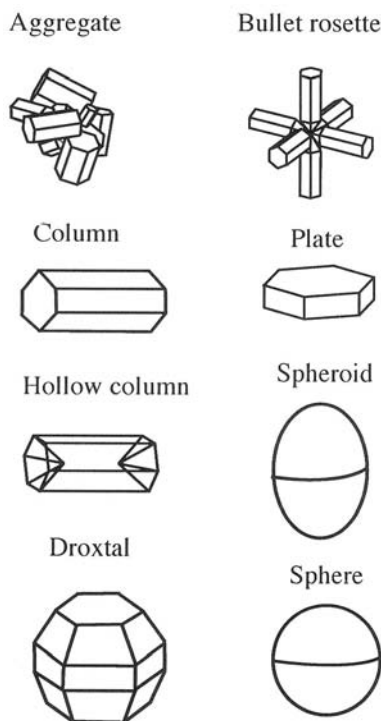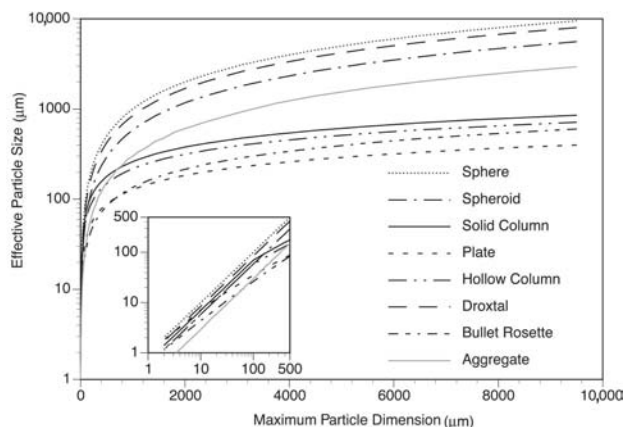
Fig. 2. Effective size versus maximum dimension for various habits.

for a maximum dimension of 50 μm, the effective size ranking is sphere, droxtal, solid column, spheroid, hollow column, plate, bullet rosette, and aggregate. As particle sizes increase, the D_e values for solid and hollow columns, plates, and bullet rosettes become much smaller than their maximum dimensions because these habits are less compact in comparison with spheres.

Figure 3 shows the complex refractive index of ice compiled by Warren[36] for a spectral region from 3 to 100 μm. The circles indicate the wavelengths for which the optical properties are computed in this study. Detailed light-scattering computations are performed at 49 discrete wavelengths that properly account for the sharp gradients in the refractive index at several spectral bands. The computed results at these wavelengths form the database. In turn, the scattering parameters can be developed at a higher spectral resolution through interpolation if required.
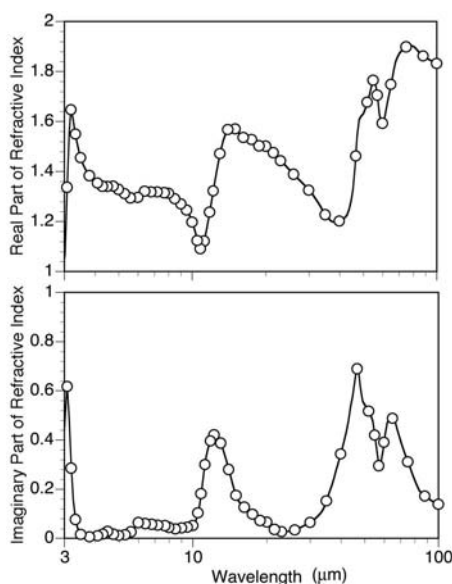
At present, there is no single method that can be used to compute the single-scattering properties for nonspherical ice particles with arbitrary sizes and shapes. The FDTD method[12,14,30] has been applied to a variety of habits. However, the application of the FDTD method to cases in which size parameters are larger than 20 is computationally impractical because of the requirements of computer CPU time and memory. When large size parameters are involved, the ray-tracing method is normally used. At IR wavelengths, a discontinuity exists between the FDTD and the IGOM solutions at a size parameter of approximately 20. Fu et al.[2,3] and Baran et al.[37] attributed this discontinuity to the tunneling effect[38,39] that is neglected in the ray-tracing approach.

Yang et al.[19] proposed the stretched scattering potential method (SSPM) to overcome the discontinuity at these intermediate size parameters. However, the SSPM is limited to the hexagonal ice particle habit and has not been modified for application to more-complex habits such as bullet rosettes or aggregates. At present, a rigorous method is unavailable to accurately bridge the gap between small and large size parameters at the IR wavelengths. Although Mitchell[40,41] has developed a modified anomalous diffraction approximation to derive approximate solutions for the extinction and absorption efficiencies, it does not provide information regarding the phase function or asymmetry factor.

Figure 4 shows the extinction efficiencies, absorption efficiencies, and asymmetry factors for hollow columns at a wavelength of 15 μm. The particle sizes are specified in terms of their maximum dimension. When the maximum dimension of a hollow column increases to more than 1000 μm, the single-scattering properties derived from the different methods converge. From Fig. 4, it is evident that the

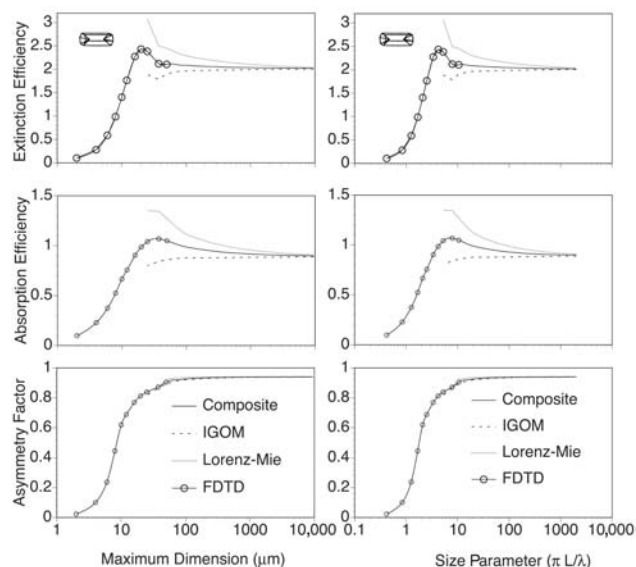

Fig. 3. Complex refractive index of ice. Data are taken from Warren.[36]

Fig. 4. Single-scattering properties of hollow columns from the composite method based on the FDTD, IGOM, and Lorenz–Mie solutions (λ = 15 μm).

equivalent-spherical solution overestimates the extinction and absorption efficiencies, whereas the IGOM underestimates the extinction and absorption efficiencies.

To resolve the issue regarding the discontinuity between the FDTD and the IGOM results at the IR wavelengths, Fu et al.[2] developed a composite method that is based on a linear combination of the equivalent-spherical solution and the IGOM nonspherical solution for moderate and large size parameters. The weighting coefficients used to combine the two solutions are properly selected so that a smooth transition from the FDTD solution to the composite solution is achieved (see Appendix A). In terms of methodology, the composite method is similar to that proposed by Liou et al.[1] in the sense that different scattering computational methods are applied to different size parameter regions. Note that Liou et al.[1] directly combined the FDTD and IGOM results for small and large size parameters, respectively. Their approach is approximately applicable at short wavelengths. For the present implementation of the composite method, the composite results combine the results from the FDTD, IGOM, and Lorenz–Mie methods, as was done by Fu et al.[2,3] To apply the Lorenz–Mie theory, nonspherical particles are usually converted into a sphere with equivalent volume, equivalent projected area, or equivalent ratio of volume to projected area. For the Lorenz–Mie solution involved in the present implementation of the composite method, the volume-based equivalence is used for the composite solutions for hollow columns and plates, whereas the equivalence based on volume-to-projected-area ratio is applied to other habits. We use the FDTD technique for ice particles (except for spheroids) with size parameters less than 20; the composite results are used for larger size parameters. As for spheroids, we employ the T-matrix method[31] to compute the single-scattering properties for small and moderate size parameters with an aspect ratio of 2. The composite method is applied to compute the extinction efficiencies, absorption efficiencies, and asymmetry factors for seven nonspherical particles with intermediate to large size parameters. The solid curves in Fig. 4 represent the results from the composite method for hollow columns at a wavelength of 15 μm. Note that the transition from the FDTD solution to the composite results is continuous. At present, there is no exact computationally efficient method available to test or validate the accuracy of the composite results for complex particles (e.g., aggregates and bullet rosettes) with size parameters between ~25 and 60.

A similar approach is used for the derivation of the scattering phase function. However, the composite method is not applicable to the phase function computation. The relative angular distribution of the scattered energy (i.e., the normalized phase function) computed from IGOM is reasonably accurate[42] for large particles at the IR wavelengths because strong absorption is involved and the phase function is quite featureless. For this reason, one should interpret the

phase functions computed from the IGOM as approximate solutions for large size parameters. For small size parameters (size parameters smaller than 20), the phase functions from FDTD are employed. For the present study, the scattering phase functions for each habit are computed at 498 scattering angles from 0° to 180°.

3. Results

Figure 5 shows the extinction efficiency, absorption efficiency, and asymmetry factor as functions of wavelength and habit for a case where the particle maximum dimension is fixed at 10 μm. For comparison, results are included for spherical ice particles. For clarity in Figs. 5–8, the results for eight ice particle habits are displayed in two columns. The panels in the left columns show the results for aggregates, solid columns, spheres, and bullet rosettes, whereas the panels in the right columns show results for droxtals, hollow columns, plates, and spheroids. In Fig. 5 the variation of the single-scattering properties with wavelength depends on the refractive index shown in Fig. 3. As such, the overall variation of the single-scattering properties versus wavelength is similar for the different habits.
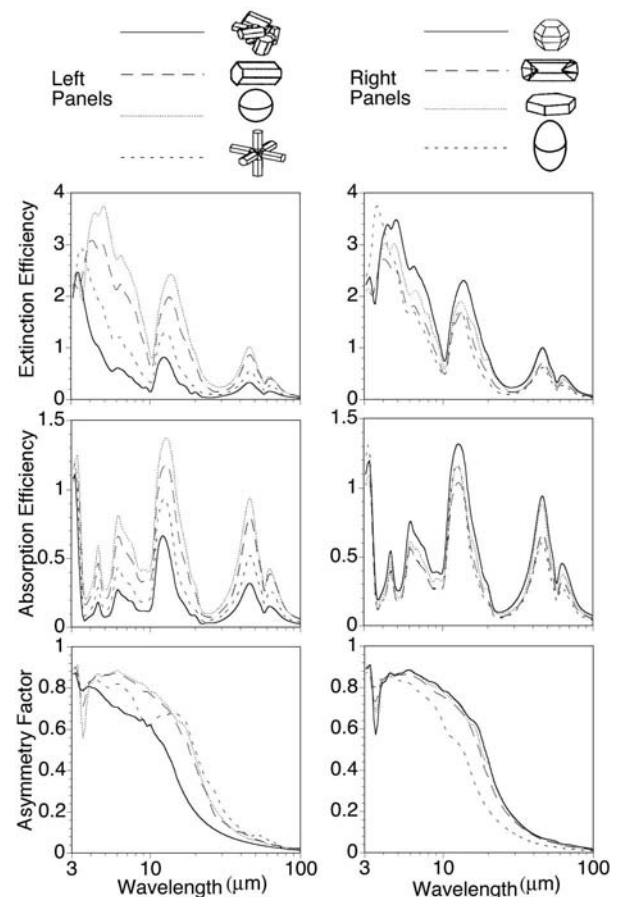

Fig. 5. Variations of extinction efficiency, absorption efficiency, and asymmetry factor for various habits for a maximum particle dimension of 10 μm.
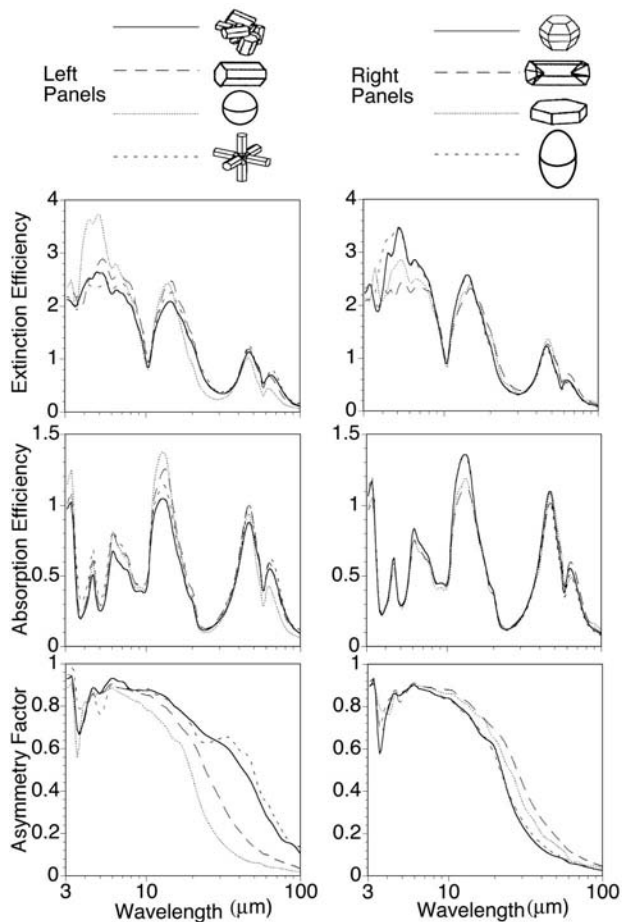
Fig. 6. Variations with wavelength of extinction efficiency, absorption efficiency, and asymmetry factors for various habits for a fixed effective size of 10 μm.
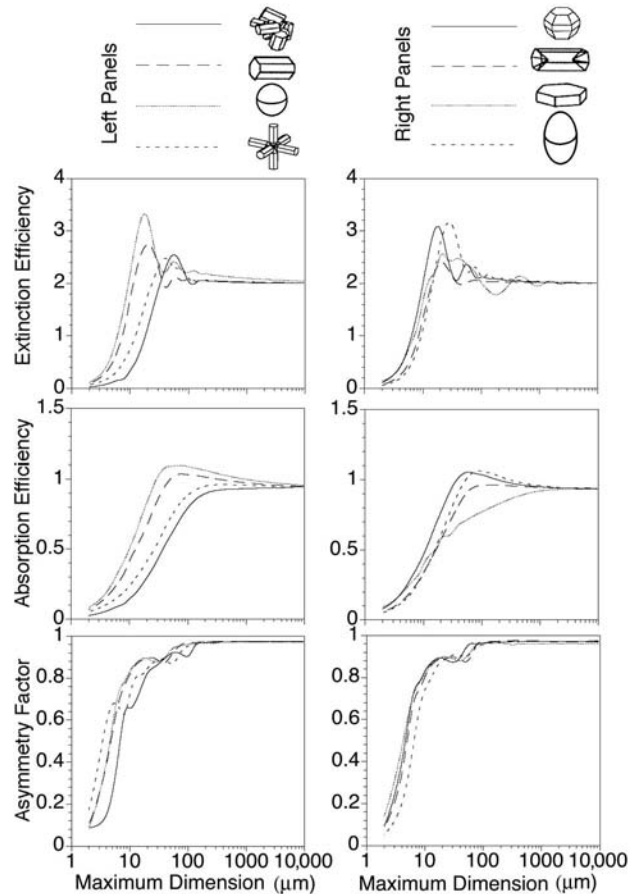

Fig. 7. Variations of extinction efficiency, absorption efficiency, and asymmetry factor as functions of maximum dimension for various habits at a fixed wavelength of 8 μm.

For each habit, there are several maxima in the extinction and absorption efficiencies that are associated primarily with the spectral variation of the refractive index of ice. In particular, the absorption efficiency has a strong correlation with the imaginary part of the refractive index (see Fig. 3). There is a general tendency for the asymmetry factor to decrease with increasing wavelength, which is due to the fact that the size parameter of a particle decreases with increasing wavelength for a given particle size, leading to a decreased amount of forward scattering in the phase function. Different habits have substantially different extinction and absorption efficiencies at a given wavelength due to the differences in particle volume, effective size, and shape. With a fixed maximum dimension of 10 μm, the spherical particle has the largest volume and effective particle size whereas the corresponding parameters for the aggregate are the smallest (see Fig. 2) by comparison. More generally, the extinction and absorption efficiencies of the spherical particles are larger than those for the other habits at most wavelengths, whereas the extinction and absorption efficiencies of the aggregate are the smallest.

Figure 6 shows the extinction efficiency, absorption efficiency, and asymmetry factor as functions of wavelength for eight particle shapes with a fixed particle size of 10 μm that is specified in terms of the effective particle size rather than the particle maximum dimension as in the previous discussion. The variation of the extinction and absorption efficiencies for the different habits are more similar for the case with a given effective particle size than for the case with a given ice particle maximum dimension, as is evident from a comparison of Figs. 5 and 6. However, at wavelengths with strong absorption, such as at wavelengths of 3.2, 12.2, and 46.7 μm, significant differences are still noted in the extinction and absorption efficiencies between the different habits. Part of these differences may be attributed to the tunneling effect discussed by Baran et al.[13] and Mitchell et al.[39] The latter authors also discussed the contribution of photon tunneling to extinction and absorption efficiencies for nonspherical particles. The rank in absorption efficiency at 12.2 μm in Fig. 6 is sphere, droxtal, spheroid, solid column, plate, hollow column, bullet rosette, and aggregate.

Figure 7 shows the variation of the single-scattering properties for various habits with parti-

cle maximum dimension at a wavelength of 8 μm. The single-scattering properties increase with maximum dimension up to sizes of approximately 20 μm for extinction efficiency and 50 μm for absorption efficiency and asymmetry factor. The extinction efficiencies oscillate around a value of 2 as the particle size increases further. There are several resonance maxima in the extinction efficiencies, but the locations and magnitude of the extinction and absorption maxima are different for each habit. The single-scattering properties of these ice particles converge to the asymptotic limits given by the geometrical-optics solution when the maximum dimension is large. For example, the extinction efficiencies for very large particles ($D > 1000$ μm) converge to 2, and the absorption coefficients converge to 0.94, which are the asymptotic values computed from the geometrical-optics method. The asymmetry factor generally increases with particle size. From Fig. 7 it is evident that, given the same particle maximum dimension, spherical particles have the largest absorption at this wavelength among all the habits.

Figure 8 is similar to Fig. 7, except that the optical properties are defined as functions of effective parti-

cle size rather than maximum dimension. From a comparison of the results in Figs. 7 and 8, the differences between the extinction (and also absorption) efficiencies for various habits are smaller if the effective particle size is used, particularly for the cases with small values of the effective particle size. Although the overall variation of the single-scattering properties with the effective particle size is similar between these habits, there still are significant differences in the resonance regions. The ranking in absorption efficiency for an effective particle size of 40 μm in Fig. 8 is sphere, droxtal, spheroid, solid column, hollow column, bullet rosette, aggregate, and plate. The extinction and absorption efficiencies for spherical particles generally are larger than those of the other habits. This seems to indicate that the assumption of spherical ice particles in the near-IR through far-IR region is generally not optimal for radiative transfer computations.

Figure 9 shows the contours of the extinction efficiency, absorption efficiency, and asymmetry factor as functions of wavelength and maximum dimension for three habits: solid columns, droxtals, and aggregates. The extinction and absorption efficiencies are dependent on the incident wavelength and the sizes and shapes of these ice particles. The absorption efficiency is strongly related to the imaginary part of the refractive index of ice. In general, the asymmetry factor increases with particle size and decreases with wavelength.

Figure 10 shows the scattering phase functions at a wavelength of 10 μm for three particle habits (aggregate, solid column, and bullet rosette) having a maximum dimension of 50 μm (top panel) and an effective size of 50 μm (bottom panel). For a fixed maximum dimension, differences are noted between bullet rosettes and the other two habits because of different volumes of these particles for a given maximum dimension and therefore a different effective particle size. For habits of a fixed effective particle size, the scattering phase functions are quite similar. Compared with those computed at the visible wavelengths,[9,18,33] phase functions in the IR region are essentially featureless in the side-scattering and backscattering directions. This behavior can be attributed to substantial absorption within the ice particles at the IR wavelengths.
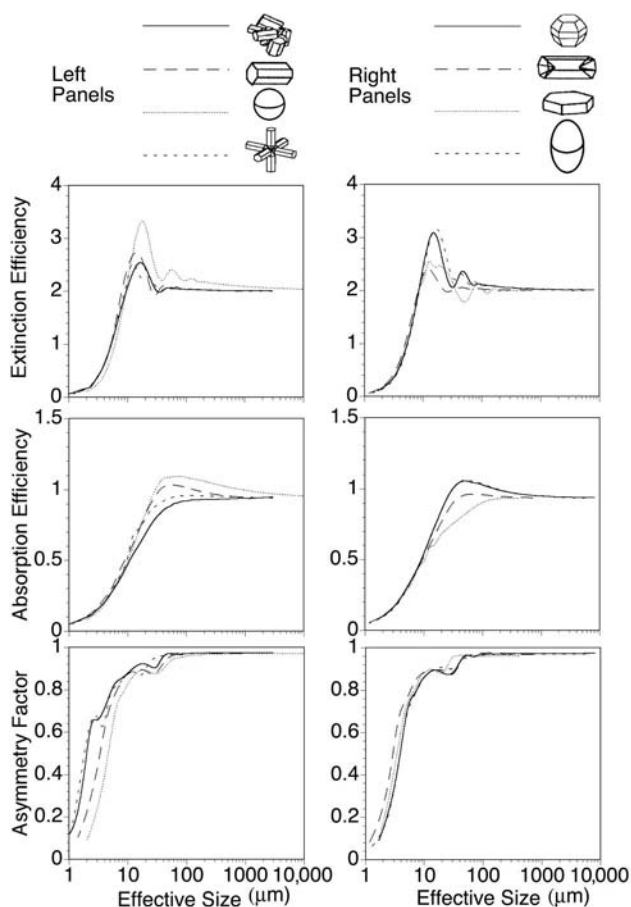

Fig. 8. Extinction efficiency, absorption efficiency, and asymmetry factor as functions of effective size for various habits at a fixed wavelength of 8 μm.

4. Bulk Optical Properties of Cirrus Clouds and Parameterization

In this section the single-scattering properties for individual particles, discussed in Section 3, are integrated over particle size distributions that are representative of mid-latitude cirrus clouds. The mean (or bulk) optical properties for a given particle size distribution $n(L)$ and habit distribution [i.e., a fractional percentage of each ice particle habit $f_i(L)$] are determined as follows:
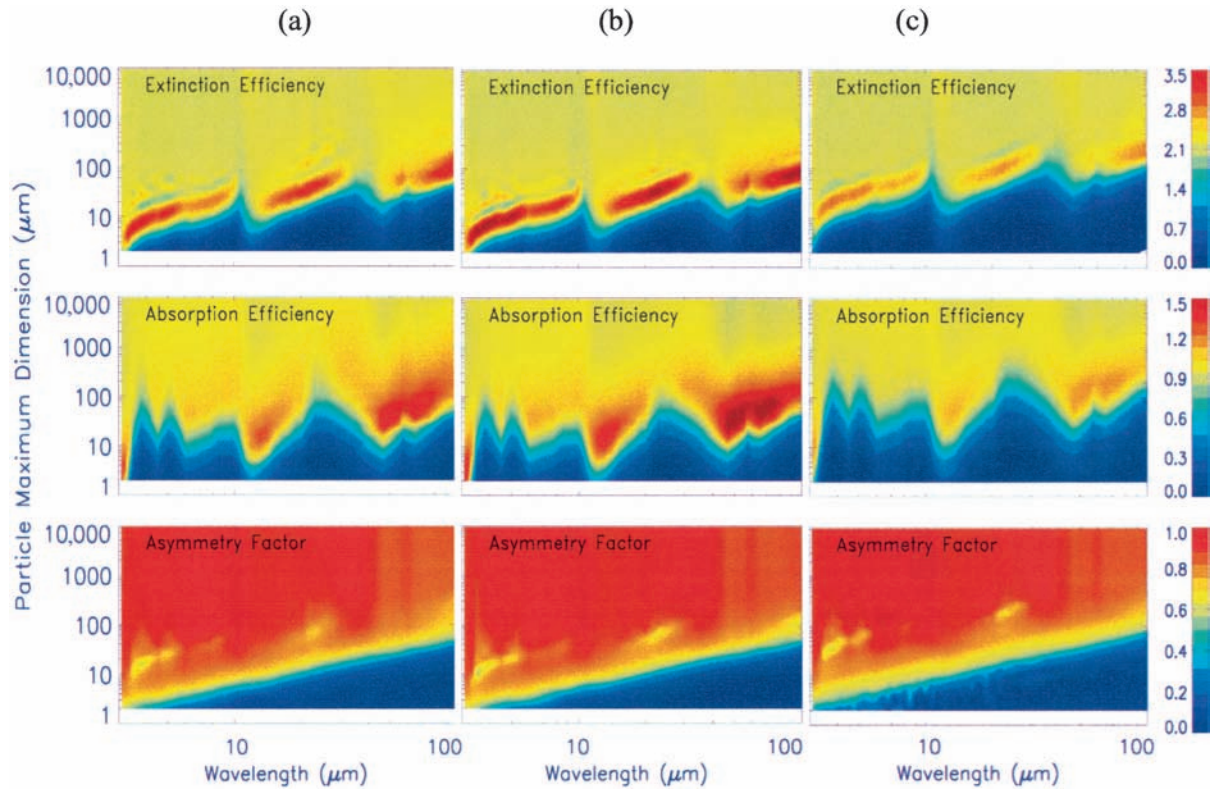
Fig. 9. Contours of extinction efficiency, absorption efficiency, and asymmetry factor as functions of wave number and the maximum dimension for solid columns [panels in column (a)], droxtals [panels in column (b)], and aggregates [panels in column (c)].
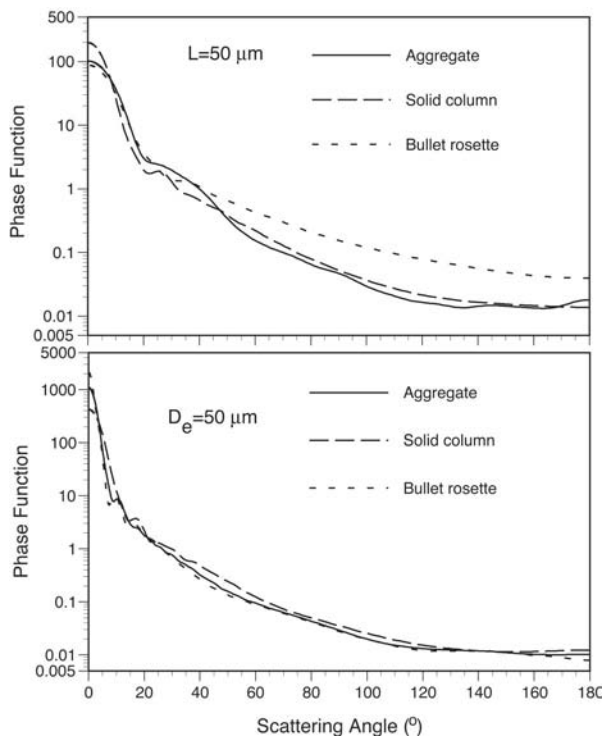
Fig. 10. Phase functions for various habits with the same maximum dimension of 50 μm (top panel) and with the same effective size (bottom panel) of 50 μm at a wavelength of 10 μm.

$$\langle Q_e \rangle = \frac{\int_{L_{\min}}^{L_{\max}} \left[\sum_{i=1}^{N} f_i(L) Q_{ei}(L) A_i(L) \right] n(L) \mathrm{d}L}{\int_{L_{\min}}^{L_{\max}} \left[\sum_{i=1}^{N} f_i(L) A_i(L) \right] n(L) \mathrm{d}L}, \qquad (2)$$

$$\langle Q_a \rangle = \frac{\int_{L_{\min}}^{L_{\max}} \left[\sum_{i=1}^{N} f_i(L) Q_{ai}(L) A_i(L) \right] n(L) \mathrm{d}L}{\int_{L_{\min}}^{L_{\max}} \left[\sum_{i=1}^{N} f_i(L) A_i(L) \right] n(L) \mathrm{d}L}, \qquad (3)$$

$$\langle g \rangle = \frac{\int_{L_{\min}}^{L_{\max}} \left[\sum_{i=1}^{N} f_i(L) g_i(L) Q_{si}(L) A_i(L) \right] n(L) \mathrm{d}L}{\int_{L_{\min}}^{L_{\max}} \left[\sum_{i=1}^{N} f_i(L) Q_{si}(L) A_i(L) \right] n(L) \mathrm{d}L}, \qquad (4)$$

$$\langle \omega \rangle = \frac{\int_{L_{\min}}^{L_{\max}} \left[\sum_{i=1}^{N} f_i(L) Q_{si}(L) A_i(L) \right] n(L) \mathrm{d}L}{\int_{L_{\min}}^{L_{\max}} \left[\sum_{i=1}^{N} f_i(L) Q_{ei}(L) A_i(L) \right] n(L) \mathrm{d}L} = 1 - \frac{\langle Q_a \rangle}{\langle Q_e \rangle}, \qquad (5)$$

Fig. 11. Bulk extinction efficiency, absorption efficiency, and asymmetry factor calculated for the 21 size distributions observed for mid-latitude cirrus clouds (circles). The solid curves are the parameterizations based on Eqs. (7)–(9).
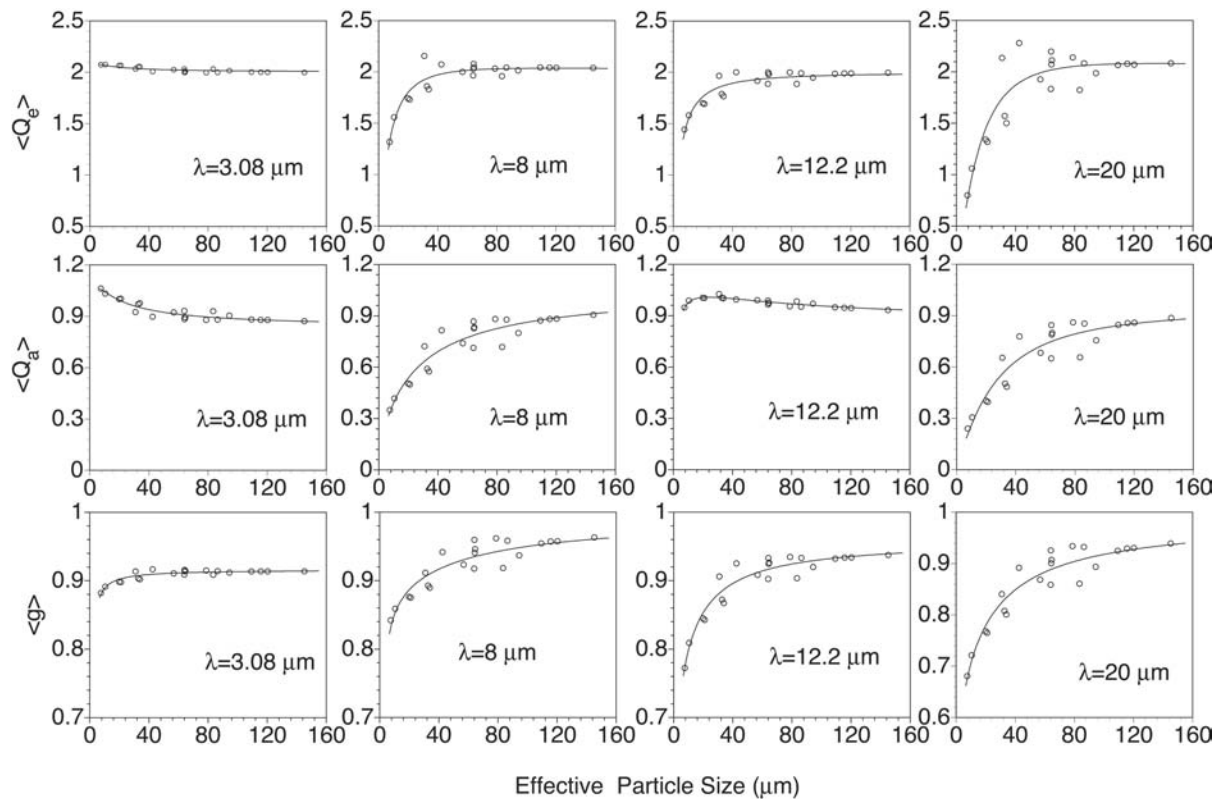
where $\langle Q_e \rangle$, $\langle Q_a \rangle$, $\langle g \rangle$, and $\langle \omega \rangle$ are the mean extinction efficiency, mean absorption efficiency, mean asymmetry factor, and mean single-scattering albedo, respectively; and N is the number of habits in an ice cloud. $Q_s(L) = Q_e(L) - Q_a(L)$ is the scattering efficiency; and $Q_e(L)$ and $Q_a(L)$ are the extinction and absorption efficiencies, respectively, calculated for individual ice particles whose maximum dimensions are denoted by L. In Eqs. (2)–(5), A is the particle projected area, and L_{min} and L_{max} are the minimum and maximum sizes in the size distribution.

Following Foot,[43] Francis *et al.*,[44] and Fu,[45] the effective particle size, defined in Eq. (1) for an individual particle, can be extended for an ice cloud with a given size distribution and fractional habit amount (f_i, where i is the habit) as follows:

$$D_e = \frac{3}{2} \frac{\int_{L_{min}}^{L_{max}} \left[\sum_{i=1}^{N} f_i(L) V_i(L) \right] n(L) \mathrm{d}L}{\int_{L_{min}}^{L_{max}} \left[\sum_{i=1}^{N} f_i(L) A_i(L) \right] n(L) \mathrm{d}L}. \quad (6)$$

The habit fraction f_i is defined such that $\sum_{l=1}^{N} f_i = 1$ at each particle size L, where N is the total number of habits.

To represent mid-latitude cirrus clouds, a set of 21 size distributions used in Fu[45] and Fu *et al.*[2] are used

to develop the bulk single-scattering properties. These size distributions were measured in a variety of mid-latitude cirrus clouds during several field campaigns. The sources of the data sets for these size distributions are explained in Fu[45] and Fu *et al.*[2]

As pointed out by King *et al.*,[46] insufficient information exists concerning ice habits and their typical percentages for any given size distribution. On the basis of available *in situ* observations, their study assumed that the mid-latitude cirrus clouds consist of 50% bullet rosettes, 25% hollow columns, and 25% plates when the maximum dimension of an ice particle is smaller than 70 μm. For larger particles, they assumed that bullet rosettes and aggregates dominate the particle size distribution, where the particles are composed of 30% aggregates, 30% bullet rosettes, 20% hollow columns, and 20% plates. The assumed ice crystal habit percentages have also been discussed in Baum *et al.*[47] We use the same habit mixture to derive the mean single-scattering properties and the parameterizations of mid-latitude cirrus clouds. The shape and aspect ratio of individual crystals in an aggregate is important to the scattering–absorption properties of the particle. It is not known at present whether there is a more realistic approximation for such a complex particle than using solid columns as employed in the previous study.

Figure 11 shows the mean extinction efficiencies, absorption efficiencies, and asymmetry factors as functions of effective particle size for four wave-

Table 1. Fitting Coefficients in Eqs. (7)–(9) for the Bulk Single-Scattering Properties of Mid-Latitude Cirrus Clouds

λ (μm)	η_1	η_2	η_3	ξ_0	ξ_1	ξ_2	ξ_3	ζ_0	ζ_1	ζ_2	ζ_3
3.08	23.33	10.85	0.95	0.834	18.58	15.16	6.33	0.916	83.92	91.93	27.88
3.20	25.53	9.31	10.35	0.832	41.95	37.19	1.41	0.940	72.16	79.20	27.08
3.33	9.46	1.94	12.39	0.904	60.88	62.99	64.88	0.970	17.78	21.47	5.55
3.50	37.59	14.56	6.22	1.025	5.93	27.76	19.02	0.987	16.31	23.16	4.29
3.80	31.26	10.62	22.28	1.050	2.96	61.78	51.09	0.982	29.66	38.26	19.17
4.10	10.68	2.15	19.56	1.071	7.70	54.25	139.20	0.995	44.97	54.27	33.96
4.30	20.33	6.88	24.08	1.057	8.10	39.98	71.11	0.995	28.33	35.39	6.95
4.50	21.79	7.25	27.17	1.034	11.99	32.21	82.69	0.995	42.08	48.19	28.41
4.75	49.97	19.35	45.48	1.056	4.00	38.82	15.15	0.987	20.60	26.14	2.69
5.00	60.09	23.60	62.69	1.064	5.68	53.39	132.49	0.987	21.24	27.13	2.30
5.30	45.07	18.15	59.14	1.070	5.90	48.59	104.57	0.987	24.34	30.22	2.13
5.60	57.53	24.60	88.00	1.046	3.84	29.60	11.76	0.995	53.28	59.95	30.08
6.00	97.06	44.73	144.00	1.018	17.02	28.85	78.68	0.985	29.00	32.20	18.62
6.40	75.49	33.00	121.86	1.012	14.44	27.00	74.66	0.998	54.43	60.00	36.88
6.80	99.72	44.46	168.53	1.028	6.07	20.79	11.08	0.998	54.56	60.46	37.20
7.20	95.59	42.37	184.14	1.019	6.56	21.93	27.95	0.985	29.53	33.67	20.00
7.70	99.29	44.63	234.49	1.046	14.52	33.89	124.18	0.995	44.53	50.83	28.78
8.00	99.72	44.72	257.19	1.056	8.68	31.90	70.58	0.995	45.80	52.65	28.74
8.50	99.00	44.51	358.12	1.064	6.30	35.08	66.37	0.995	50.22	57.69	31.32
9.00	99.77	44.99	472.22	1.072	7.29	35.77	82.92	0.995	45.52	52.11	29.00
9.50	94.29	42.56	611.35	1.066	4.71	32.79	45.55	0.987	37.01	41.58	28.94
10.00	88.50	39.59	936.09	1.111	5.45	36.94	23.67	0.995	76.35	81.21	83.90
10.50	99.04	52.15	1250.54	1.073	9.97	28.43	41.74	0.991	91.30	93.51	121.69
10.80	91.55	57.10	680.44	1.033	27.33	38.10	97.29	0.996	39.97	42.69	53.09
11.20	7.39	11.92	14.14	0.953	67.55	70.43	131.93	0.988	37.72	42.24	47.94
11.80	87.80	46.59	193.12	0.870	83.12	77.94	95.58	0.975	24.01	29.11	25.23
12.20	85.22	43.54	149.15	0.855	81.19	73.30	87.29	0.960	7.84	11.54	3.11
13.00	99.37	47.04	155.60	0.838	81.86	71.83	111.61	0.958	8.84	13.26	2.81
14.00	98.47	42.51	193.18	0.858	92.50	83.58	229.23	0.981	41.54	50.97	56.52
15.00	99.86	40.78	260.59	0.919	92.00	89.95	476.70	0.985	23.56	31.79	24.97
16.20	99.18	39.70	392.39	0.960	91.32	94.27	891.45	0.994	35.96	45.71	57.28
17.50	98.89	38.33	492.45	0.965	91.98	98.24	1382.35	0.988	15.35	23.94	5.24
18.80	99.32	36.59	707.69	0.945	72.08	77.54	1887.23	0.995	13.81	22.53	5.77
20.00	88.31	31.76	730.02	0.946	60.81	68.44	1901.77	0.987	13.12	21.77	8.19
21.50	47.62	13.38	677.86	0.953	25.87	56.40	1765.68	0.990	17.87	29.40	7.34
23.00	30.71	4.86	761.98	0.965	13.00	65.21	1426.66	0.979	16.59	26.83	16.42
26.00	31.47	0.06	1194.78	0.980	17.12	68.37	1688.58	0.982	43.75	55.52	136.15
30.00	29.73	0.17	1597.60	0.982	30.86	58.80	1933.24	0.973	90.60	97.75	409.89
35.00	52.95	26.32	1999.19	1.060	65.56	82.57	1889.06	0.985	5.50	8.73	49.00
40.00	98.78	55.69	1728.50	1.028	89.13	94.47	1092.92	0.972	6.00	10.66	68.89
46.70	99.19	43.76	859.98	0.859	98.72	81.39	531.13	0.871	80.12	84.14	1024.19
52.00	99.88	34.46	1300.18	0.887	94.55	74.79	993.58	0.901	31.85	36.35	490.39
55.00	92.68	24.16	1559.57	0.845	97.81	69.00	1597.60	0.933	4.24	12.17	99.76
57.20	54.06	7.01	1545.60	0.865	69.35	45.75	1910.65	0.919	16.82	22.22	271.70
60.00	84.26	25.10	1878.09	0.880	94.93	70.12	1923.60	0.914	15.74	19.62	278.05
65.00	99.57	27.83	1841.84	0.864	99.35	70.72	1668.81	0.920	6.37	13.58	163.96
75.00	54.56	0.10	1884.74	0.840	43.21	15.27	1917.51	0.911	0.45	8.56	49.79
88.00	48.06	0.07	1998.92	0.881	13.24	5.67	1770.26	0.886	10.69	19.52	146.24
99.99	37.09	0.08	1994.25	0.920	8.51	15.65	1883.37	0.917	72.84	95.96	665.96

lengths computed for the 21 size distributions. The bulk scattering properties of ice clouds are shown to be strongly dependent on the effective particle size at each wavelength.

A parameterization of these bulk single-scattering properties is developed based on these results. The single-scattering properties are parameterized as the function of effective particle size at each wavelength as follows:

$$\langle Q_e \rangle = \frac{2 + \eta_1 D_e^{-1}}{1 + \eta_2 D_e^{-1} + \eta_3 D_e^{-2}}, \tag{7}$$

$$\langle Q_a \rangle = \frac{\xi_0 + \xi_1 D_e^{-1}}{1 + \xi_2 D_e^{-1} + \xi_3 D_e^{-2}}, \tag{8}$$

$$\langle g \rangle = \frac{\zeta_0 + \zeta_1 D_e^{-1}}{1 + \zeta_2 D_e^{-1} + \zeta_3 D_e^{-2}}, \tag{9}$$
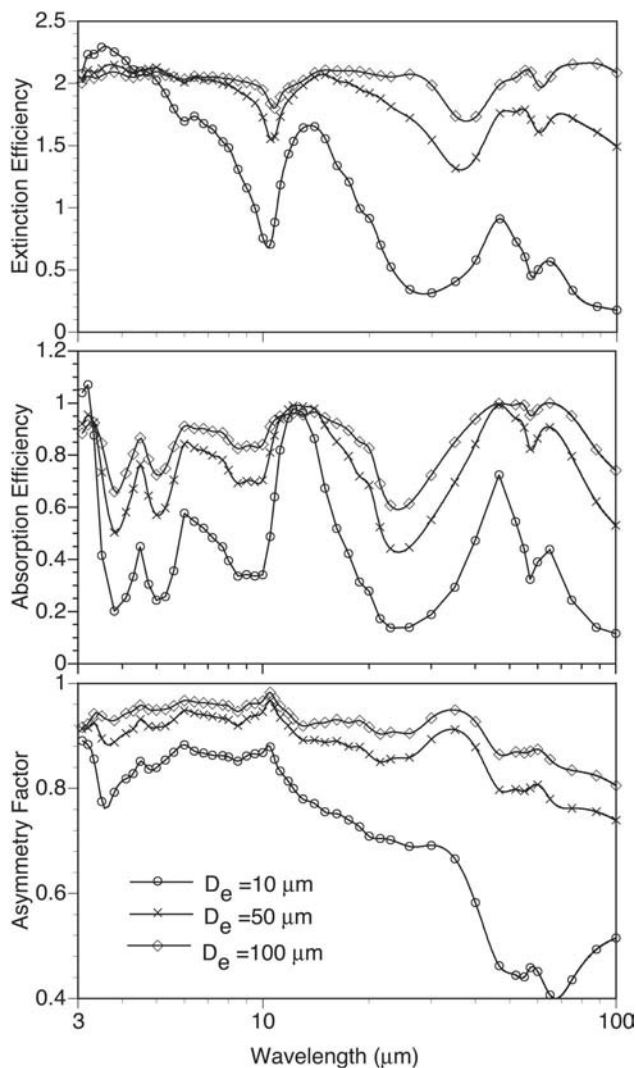
Fig. 12. Bulk single-scattering properties as functions of wavelength for three effective sizes. The symbols show the composite values at 49 discrete wavelengths; the solid curves are the interpolated results with a high spectral resolution of 0.01 μm.

dependence on the effective particle size in the IR region, particularly at small sizes, and are also sensitive to the wavelength. At the near-IR wavelengths (e.g., 3.08 μm), the extinction efficiency varies smoothly as a function of effective particle size. At longer wavelengths, the general feature to note is that the mean extinction efficiency increases monotonically with size to an asymptotic value of 2. The 3.08 and 12.2 μm wavelengths are located in strong absorption bands of ice (see the lower panel of Fig. 3), whereas the 8 and 20 μm wavelengths are located at the bands with relatively weaker absorption. The variation of absorption efficiency with effective particle size is different at strongly versus weakly absorbing wavelengths. At strongly absorbing wavelengths, the absorption efficiency decreases slightly with increasing effective particle size, whereas the absorption efficiency increases with increasing effective particle size at weakly absorbing wavelengths. This is a result of the combination of the particle size distribution with the absorption properties of the various particle habits at these wavelengths. The mean asymmetry factor increases with effective particle size at each wavelength.

The parameterization results can be easily extended for applications involving high-spectral-resolution studies through an interpolation of the fitted results based on the results for the 49 wavelengths. The symbols in Fig. 12 show the parameterized single-scattering properties as a function of wavelength for three effective particle sizes. Also shown in Fig. 12 are the results obtained through interpolation using a spline fitting technique at a spectral resolution of 0.01 μm. The interpolation does not incur noticeable errors.

5. Summary

The single-scattering properties of ice particles in the near-infrared through far-infrared wavelength regime are computed from a composite method that is based on the FDTD technique, the T-matrix method, an IGOM, and the Lorenz–Mie theory for equivalent ice spheres. Seven nonspherical ice crystal habits (aggregates, hexagonal hollow and solid columns, plates, 3D bullet rosettes, spheroids, and droxtals) are considered in the present study. A database of the single-scattering properties for each of these ice particle habits has been developed at 49 discrete wavelengths between 3 and 100 μm and for particle sizes ranging from 2 to 10,000 μm in terms of the particle maximum dimension. The dependence of the single-scattering properties on the particle maximum dimension and effective particle size are also discussed. Finally, a parameterization of the bulk optical properties is developed for mid-latitude cirrus clouds based on 21 particle size distributions obtained from various field campaigns.

Appendix A: Composite Method

In the present study, the derivation of the ice particle scattering property database employs a composite method developed by Fu et al.[2,3] For completeness, we

where η_i, ξ_i, and ζ_i ($i = 0, 1, 2, 3$) are fitting coefficients that are functions of wavelength. These coefficients are determined using the Monte Carlo technique. The parameterization scheme provided in Eqs. (7)–(9) has some advantages as compared with the conventional parameterization scheme based on polynomials. For example, when D_e is large, the parameterized extinction efficiency given by Eq. (7) approaches 2, the asymptotic value for large particles, whereas it approaches zero for small particles. This parameterization approach has physically correct limits that are expected from scattering theory. Table 1 lists these fitting coefficients for the 49 wavelengths used in the database. As an example, the parameterization results for the single-scattering properties at the four wavelengths are also shown in Fig. 11 (solid curves).

It is evident from Fig. 11 that the single-scattering properties for each size distribution have a strong

briefly present the theoretical framework of this method. Basically, the composite method combines results for the scattering properties (e.g., the extinction efficiency, absorption efficiency, and asymmetry factor) computed from the IGOM, Lorenz–Mie, and FDTD methods (see Fig. 4). As an example, the composite result for absorption efficiency at wavelength λ is as follows:

$$Q_a(L) = \begin{cases} Q_{a\text{FDTD}}(L) & (L < 20\lambda/\pi) \\ C_1 Q_{a\text{Mie}}(L) + C_2 Q_{a\text{IGOM}}(L) & (L \geq 20\lambda/\pi), \end{cases}$$
$$(A1)$$

where $Q_a(L)$, $Q_{a\text{FDTD}}(L)$, $Q_{a\text{Mie}}(L)$, and $Q_{a\text{IGOM}}(L)$ are absorption coefficients computed from the composite method, FDTD, the Lorenz–Mie theory, and IGOM, respectively. The weighting coefficients C_1 and C_2 in Eq. (A1) are determined so that a smooth transition is achieved from the FDTD solution to the composite solution, i.e.,

$$Q_{a\text{FDTD}}(L_c) = C_1 Q_{a\text{Mie}}(L_c) + C_2 Q_{a\text{IGOM}}(L_c), \quad (A2)$$

where L_c is the largest maximum dimension derived from the FDTD method. The coefficients C_1 and C_2 are dependent on both wavelength and ice particle habit. The composite method results for the hollow column habit at a wavelength of 15 μm is shown in Fig. 4. A similar approach is used to compute extinction efficiencies and asymmetry factors at each wavelength for each ice particle habit.

References

1. K. N. Liou, Y. Takano, and P. Yang, "Light scattering and radiative transfer by ice crystal clouds: applications to climate research," in *Light Scattering by Nonspherical Particles: Theory, Measurements, and Geophysical Applications*, M. I. Mishchenko, J. W. Hovenier, and L. D. Travis, eds. (Academic, 2000), pp. 417–449.
2. Q. Fu, P. Yang, and W. B. Sun, "An accurate parameterization of the infrared radiative properties of cirrus clouds for climate models," J. Clim. **25,** 2223–2237 (1998).
3. Q. Fu, W. B. Sun, and P. Yang, "On model of scattering and absorption by cirrus nonspherical ice particles at thermal infrared wavelength," J. Atmos. Res. **56,** 2937–2947 (1999).
4. H. Chepfer, P. Goloub, J. Riedi, J. De Haan, J. W. Hovenier, and P. H. Flamant, "Ice crystal shapes in cirrus clouds derived from POLDER-1/ADEOS-1," J. Geophys. Res. **106,** 7955–7966 (2001).
5. A. J. Baran, "Simulation of infrared scattering from ice aggregates by use of a size-shape distribution of circular ice cylinders," Appl. Opt. **42,** 2811–2818 (2003).
6. P. Minnis, P. W. Heck, and D. F. Young, "Inference of cirrus cloud properties from satellite observed visible and infrared radiances. Part II: Verification of theoretical radiative properties," J. Atmos. Sci. **50,** 1305–1322 (1993).
7. J. Reichardt, S. Reichardt, M. Hess, and T. J. McGee, "Corrections among the optical properties of cirrus-cloud particle microphysical interpretation," J. Geophys. Res. **107,** 4562, 10.1029/2002JD002589 (2002).
8. M. I. Mishchenko, W. B. Rossow, A. Macke, and A. A. Lacis, "Sensitivity of cirrus cloud albedo, bidirectional reflectance and optical thickness retrieval accuracy to ice particle shape," J. Geophys. Res. **101,** 16973–16985 (1996).
9. Y. Takano and K. N. Liou, "Solar radiative transfer in cirrus clouds. Part I. Single-scattering and optical properties of hexagonal ice crystals," J. Atmos. Sci. **46,** 3–19 (1989).
10. Y. Takano and K. N. Liou, "Radiative transfer in cirrus clouds. III. Light scattering by irregular ice crystals," J. Atmos. Sci. **52,** 818–837 (1995).
11. A. Macke, J. Mueller, and E. Raschke, "Single scattering properties of atmospheric ice crystal," J. Atmos. Sci. **53,** 2813–2825 (1996).
12. W. Sun, Q. Fu, and Z. Chen, "Finite-difference time-domain solution of light scattering by dielectric particles with perfectly matched layer absorbing boundary conditions," Appl. Opt. **38,** 3141–3151 (1999).
13. A. J. Baran, S. Haveman, P. N. Francis, and P. Yang, "A study of the absorption and extinction properties of hexagonal ice columns and plates in random and preferred orientation, using exact T-matrix theory and aircraft observations of cirrus," J. Quant. Spectrosc. Radiat. Transfer **70,** 505–518 (2001).
14. P. Yang and K. N. Liou, "Finite-difference time domain method for light scattering by small ice crystals in three-dimensional space," J. Opt. Soc. Am. A **13,** 2072–2085 (1996).
15. K. Muinonen, "Scattering of light by crystals: a modified Kirchhoff approximation," Appl. Opt. **28,** 3044–3050 (1989).
16. A. Macke, "Monte Carlo calculations of light scattering by large particles with multiple internal inclusions," in *Light Scattering by Nonspherical Particles: Theory, Measurements, and Applications*, M. I. Mishchenko, J. W. Hovenier, and L. D. Travis, eds., (Academic, 2000), pp. 309–322.
17. P. Yang and K. N. Liou, "Geometric-optics-integral-equation method for light scattering by nonspherical ice crystals," Appl. Opt. **35,** 6568–6584 (1996).
18. P. Yang, K. N. Liou, K. Wyser, and D. Mitchell, "Parameterization of scattering and absorption properties of individual ice crystals," J. Geophys. Res. **105,** 4699–4718 (2000).
19. P. Yang, B. C. Gao, B. A. Baum, Y. X. Hu, W. J. Wiscombe, S. C. Tsay, D. M. Winker, and S. L. Nasiri, "Radiative properties of cirrus clouds in the infrared (8–13 μm) spectral region," J. Quant. Spectrosc. Radiat. Transfer **70,** 473–504 (2001).
20. P. Yang, B. A. Baum, A. J. Heymsfield, Y. X. Hu, H.-L. Huang, S.-C. Tsay, and S. Ackerman, "Single-scattering properties of droxtals," J. Quant. Spectrosc. Radiat. Transfer **79–80,** 1159–1180 (2003).
21. P. Yang, M. G. Mlynczak, H. L. Wei, D. P. Kratz, B. A. Baum, Y. X. Hu, W. J. Wiscombe, A. Heidinger, and M. I. Mishchenko, "Spectral signature of ice clouds in the far-infrared region: single-scattering calculations and radiative sensitivity study," J. Geophys. Res. **108,** 4569, 10.1029/2002JD2002JD003291 (2003).
22. W. L. Smith, X. Ma, A. Steven, S. A. Ackerman, H. E. Revercomb, and R. O. Knuteson, "Remote sensing cloud properties from high spectral resolution infrared observations," J. Atmos. Sci. **50,** 1708–1720 (1993).
23. S. A. Ackerman, W. L. Smith, J. D. Spinhirne, and H. E. Revercomb, "The 27–28 October 1986 far-IRE IFO cirrus case study: spectral properties of cirrus clouds in the 8–12 μm window," Mon. Weather Rev. **118,** 2377–2388 (1990).
24. W. L. Smith, S. Ackerman, H. Revercomb, H. Huang, D. H. DeSlover, W. Feltz, L. Gumley, and A. Collard, "Infrared spectral absorption of nearly invisible cirrus clouds," Geophys. Res. Lett. **25,** 1137–1140 (1998).

25. A. H. Huang, P. Yang, H.-L. Wei, B. A. Baum, Y.-X. Hu, P. Antonelli, and S. A. Ackerman, "Retrieval of ice cloud properties from high spectral resolution infrared observations," IEEE Trans. Geosci. Remote Sens. **42,** 842–853 (2004).

26. H. Wei, P. Yang, J. Li, B. A. Baum, H.-L. Huang, S. Platnick, Y. X. Hu, and L. Strow, "Retrieval of semitransparent ice cloud optical thickness from Atmospheric Infrared Sounder (AIRS) measurements," IEEE Trans. Geosci. Remote Sens. **42,** 2254–2267 (2004).

27. S. Chung, S. Ackerman, P. F. Van Delst, and W. P. Menzel, "Model calculations and interferometer measurements of ice-cloud characteristics," J. Appl. Meteorol. **39,** 634–644 (2000).

28. D. H. DeSlover, W. L. Smith, P. K. Piironen, and E. W. Eloranta, "A methodology for measuring cirrus cloud visible-to-infrared spectral optical thickness ratios," J. Atmos. Oceanic Technol. **16,** 251–262 (1999).

29. A. J. Heymsfield and J. Iaquinta, "Cirrus crystal terminal velocities," J. Atmos. Sci. **5,** 916–938 (2000).

30. K. S. Yee, "Numerical solution of initial boundary problems involving Maxwell's equations in isotropic media," IEEE Trans. Antennas Propag. **14,** 302–307 (1966).

31. M. I. Mishchenko and L. D. Travis, "Capabilities and limitations of a current FORTRAN implementation of the T-matrix method for randomly oriented rotationally symmetric scatterers," J. Quant. Spectrosc. Radiat. Transfer **60,** 309–324 (1998).

32. Z. Zhang, P. Yang, G. W. Kattawar, S.-C. Tsay, B. A. Baum, H.-L. Huang, Y. X. Hu, A. J. Heymsfield, and J. Reichardt, "Geometrical-optics solution to light scattering by droxtal ice crystals," Appl. Opt. **43,** 2490–2499 (2004).

33. P. Yang and K. N. Liou, "Single-scattering properties of complex ice crystals in terrestrial atmosphere," Contrib. Atmos. Phys. **71,** 223–248 (1998).

34. T. C. Grenfell and S. G. Warren, "Representation of nonspherical ice particles by a collection of independent spheres for scattering and absorption of radiation," J. Geophys. Res. **104,** 31697–31709 (1999).

35. D. L. Mitchell, A. Macke, and Y. Liu, "Modeling cirrus clouds. Part II: Treatment of radiative properties," J. Atmos. Sci. **53,** 2967–2987 (1996).

36. S. G. Warren, "Optical constants of ice from the ultraviolet to the microwave," Appl. Opt. **23,** 1206–1225 (1984).

37. A. J. Baran, P. N. Francis, and P. Yang, "A process study of the dependence of ice crystal absorption on particle geometry: application to aircraft radiometric measurements of cirrus cloud in the terrestrial window region," J. Atmos. Sci. **60,** 417–427 (2003).

38. H. M. Nussenzveig and W. J. Wiscombe, "Diffraction as tunneling," Phys. Rev. Lett. **59,** 1667–1670 (1987).

39. D. L. Mitchell, W. P. Arnott, C. Schmitt, A. J. Baran, S. Havemann, and Q. Fu, "Contributions of photon tunneling to extinction in laboratory grown hexagonal columns," J. Quant. Spectrosc. Radiat. Transfer **70,** 761–776 (2001).

40. D. L. Mitchell, "Parameterization of the Mie extinction and absorption coefficients for water clouds," J. Atmos. Sci. **57,** 1311–1326 (2000).

41. D. L. Mitchell, "Effective diameter in radiation transfer: general definition, applications, and limitations," J. Atmos. Sci. **59,** 2330–2346 (2002).

42. Y. K. Lee, P. Yang, M. I. Mishchenko, B. A. Baum, Y. Hu, H.-L. Huang, W. J. Wiscombe, and A. J. Baran, "On the use of circular cylinders as surrogates for hexagonal pristine ice crystals in scattering calculations at infrared wavelengths," Appl. Opt. **42,** 2653–2664 (2003).

43. J. S. Foot, "Some observations of the optical properties of clouds: II. Cirrus," Q. J. R. Meteorol. Soc. **114,** 145–164 (1988).

44. P. N. Francis, A. Jones, R. W. Saunders, K. P. Shine, A. Slingo, and Z. Sun, "An observational and theoretical study of the radiative properties of cirrus: some results from ICE'89," Q. J. R. Meteorol. Soc. **120,** 809–848 (1994).

45. Q. Fu, "An accurate parameterization of the solar radiative properties of cirrus clouds for climate models," J. Clim. **9,** 2058–2082 (1996).

46. M. D. King, S. Platnick, P. Yang, G. T. Arnold, M. A. Gray, J. C. Riedi, S. A. Ackerman, and K. N. Liou, "Remote sensing of liquid water and ice cloud optical thickness, and effective radius in the arctic: application of air-borne multispectral MAS data," J. Atmos. Oceanic Technol. **21,** 857–875 (2004).

47. B. A. Baum, D. P. Kratz, P. Yang, S. C. Ou, Y. Hu, P. Soulen, and S. C. Tsay, "Remote sensing of cloud properties using MODIS Airborne Simulator imagery during SUCCESS. I: Data and models," J. Geophys. Res. **105,** 11767–11780 (2000).